The Astrophysical Journal, 577:993–1005, 2002 October 1

COMPLETE MODELS OF AXISYMMETRIC SUNSPOTS: MAGNETOCONVECTION WITH CORONAL HEATING

Neal E. Hurlburt and David Alexander
Lockheed Martin Advanced Technology Center, (L9-41), Building 252, 3251 Hanover Street, Palo Alto, CA 94304

and

Alastair M. Rucklidge
Department of Applied Mathematics, University of Leeds, Leeds LS 2 9JT, UK
Received 2002 February 19; accepted 2002 May 29

ABSTRACT

We present detailed results of numerical experiments into the nature of complete sunspots. The models remain highly idealized but include fully nonlinear compressible magnetoconvection in an axisymmetric layer that drives energy into an overlying, low-β plasma. We survey a range of parameters in which the resulting magnetoconvection displays the formation of pore- and sunspot-like behavior and assess the coronal signatures resulting from the energy generated by the magnetoconvection. The coronal heating is assumed to be a result of the dissipation by an unspecified means of a fraction of the Poynting flux entering the corona. The expected signatures in the EUV and soft X-ray bandpasses of the *Transition Region and Coronal Explorer* and *Yohkoh*/SXT, respectively, are examined. This ad hoc coupling of the corona to the subphotospheric region results in a dynamical behavior that is consistent with recent observational results. This agreement demonstrates that even simple coupled modeling can lead to diagnostics for investigations of both subphotospheric sunspot structures and coronal heating mechanisms.

Subject headings: convection — hydrodynamics — Sun: corona — Sun: magnetic fields — Sun: X-rays, gamma rays — sunspots

1. INTRODUCTION

Sunspots offer a view into the interior workings of the Sun. Features in the photosphere, from the cool umbra to the details of the penumbral structure, have long been used to deduce the underlying dynamics. As recent high-resolution observations of the solar photosphere have been made, these details have led us away from the axisymmetric models of the penumbra and the old debates about shallow or deep penumbra to models with large variations in azimuth and a much richer penumbral construction (Title et al. 1991; Lites et al. 1993). Similarly, observations of light bridges (Leka 1997), umbral dots, and penumbral grains (Sobotka, Brandt, & Simon 1997; Sobotka & Sütterlin 2001) and helioseismic observations below sunspots (Zhao, Kosovovich, & Duvall 2001) are prompting a reconsideration of the debates on the structure beneath the umbra.

Further clues reside above the solar photosphere. X-ray and EUV observations of active regions have revealed a clear relationship between the loop structure above sunspots and the photospheric structure within them. X-ray anemones rise from the penumbrae of sunspots and have azimuthal structure similar to that seen in the penumbra (e.g., Martens et al. 1996a, 1996b). EUV loops typically emanate from the penumbral-umbral boundary or light bridges within the umbra (Schrijver et al. 1999). Both these observations offer clues to the structures beneath them, but current theoretical models are inadequate for interpreting them.

Here we begin to address this problem by developing a simple, coupled model for the evolution of compressible magnetoconvection beneath the photosphere and coronal loops above it. The magnetoconvection model is based on the axisymmetric code developed by Hurlburt & Rucklidge (2000, hereafter HR) to study isolated flux tubes. Here we only modify the field configuration to be one with zero net flux, thereby capturing both footpoints of the resulting coronal loops. The coronal model assumes a quasi-static potential field that experiences heating from the motions of the magnetic field in the convecting layer beneath it. We investigate both the dynamics of the resulting magnetoconvection and the signatures of these dynamics in the coronal heating.

The coupling of the motions within and below the solar photosphere to the upper solar atmosphere allows us to explore our ability to describe and model complete solar structures such as sunspots. In this paper we will demonstrate how the structure and dynamics of sunspot penumbrae influence the structure and heating of the solar corona and, in turn, how observations of the coronal dynamics can provide clues to what is happening beneath the photosphere.

Thermal convection dominates the motions within the solar interior; the solar plasma is highly ionized and at relatively high densities, so the plasma is optically thick and the diffusion approximation is reasonable; the influence of the magnetic field, as measured by the plasma $\beta \gg 1$, is thought to be small. The solar corona is convectively stable, the density is low so the plasma is optically thin, radiative transport is dominant, and the magnetic field dominates the dynamics with $\beta \ll 1$. The transition between these two regimes occurs somewhere in the vicinity of the photosphere, and hence prior work has focused on one region or the other as separate computational domains.

Our approach is to combine distinct models of the two regimes and then couple them, to build a composite system. The subphotospheric magnetoconvection model is that of HR. The coronal field structure is defined by a

potential field specified by the surface boundary conditions of the magnetoconvection model. Coronal heating is assumed to be quasi-static with the heating rate determined from the dynamic boundary conditions at the surface. In this way, the coupling of the two regimes is achieved via the magnetic field with the upper boundary condition required by the magnetoconvection models acting as a lower boundary condition for the coronal field model and the subsequent heating of coronal loops. Future work will develop a more rigorous coupling by including feedback from the thermodynamical requirement of the corona to the magnetoconvection model.

The present paper is organized as follows: § 2 summarizes the magnetoconvection model, the equations and numerical analysis of which are detailed in § 3. We discuss the behavior of the magnetoconvection in § 4 and the extension of the boundary condition into the corona in § 5. The heating model and results appear in § 6 and a comparison with observations in § 7. We discuss our conclusions in § 8.

2. THE MODEL

The key properties that distinguish the dynamics within the convection zone from those in the corona are the plasma β, the relative densities, and the dominant means of energy transfer. In the high-density, high-β convection zone, modest, subsonic flows of a few hundred meters per second to a few kilometers per second are sufficient to dominate over the magnetic field, and energy transport then becomes a balance between the convection and thermal diffusion. In the low-density, low-β corona, flows on the order of hundreds of kilometers per second approach the local Alfvén speed, while the optically thin plasma radiates freely into space. The two regions are quite distinct in their properties, and thus proper treatment of both probably calls for different approaches. (For this discussion we have omitted the chromosphere, which is both difficult to handle and relatively thin on the scales we are considering. It must of course be included at some point, but for convenience we dismiss further discussion of it here.) Our model is an extreme case of addressing the coupling between the convection zone and corona. We ignore radiative properties within the convection zone and keep the physical properties of the fluid there quite simple. We assert that the magnetic field in our model corona dominates and that the response time to any footpoint motions is rapid compared to convective timescales. This quasi-static model takes the field to be potential at all times and assumes that the relaxation between two potential states occurs instantaneously. This provides an upper boundary condition on the magnetoconvection occurring below it. Since we are assuming that there is a large difference in density between the convecting region and the corona (which is in fact larger than that found between water and air on Earth), we further require that the mass flux out of the photosphere be zero everywhere.

Thus, our simplest model consists of a convecting layer with zero mass flux and a potential field imposed at the upper boundary. The coronal field is the potential that matches the field distribution at the boundary and that is heated by the underlying convection. The source of heating is the Poynting flux emanating from the upper boundary.

3. EQUATIONS AND NUMERICAL METHODS

We solve the partial differential equations (p.d.e.'s) that describe compressible magnetoconvection in axisymmetric geometry using the formulation and numerical code developed by HR. A layer of electrically conducting gas experiences a uniform gravitational acceleration g directed downward and possesses a shear viscosity μ, a thermal conductivity K, a magnetic diffusivity η, and a magnetic permeability μ_0, all of which are assumed to be constant. We assume that the fluid satisfies the equation of state for a perfect monatomic gas with constant heat capacities c_v and $c_p = c_v + R_*$, where R_* is the gas constant. The velocity field $\boldsymbol{u}$, magnetic field $\boldsymbol{B}$, temperature T, pressure P, and density ρ depend on time t and on the cylindrical coordinates (r, ϕ, z). The relevant p.d.e.'s are then the continuity equation,

$$\frac{\partial \rho}{\partial t} + \nabla \cdot \rho \boldsymbol{u} = 0 \,, \tag{1}$$

the compressible Navier-Stokes equation,

$$\frac{\partial \rho \boldsymbol{u}}{\partial t} + \nabla \cdot \rho \boldsymbol{u}\boldsymbol{u} = -\nabla P + \rho g \hat{z} + \frac{1}{\mu_0}(\nabla \times \boldsymbol{B}) \times \boldsymbol{B} + \mu(\nabla^2 \boldsymbol{u} + \frac{1}{3}\nabla \nabla \cdot \boldsymbol{u}) \,, \tag{2}$$

the total energy equation,

$$\rho c_v \left(\frac{\partial T}{\partial t} + \boldsymbol{u} \cdot \nabla T \right) = -P \nabla \cdot \boldsymbol{u} + K \nabla^2 T + Q_d \,, \tag{3}$$

where Q_d denotes the combined viscous and ohmic dissipation (described in HR), and the induction equation,

$$\frac{\partial \boldsymbol{B}}{\partial t} = \nabla \times (\boldsymbol{u} \times \boldsymbol{B}) + \eta \nabla^2 \boldsymbol{B} \quad \text{with} \quad \nabla \cdot \boldsymbol{B} = 0 \,. \tag{4}$$

These are augmented by the equation of state for a perfect gas, $P = R_* \rho T$.

The equations can be simplified by restricting our considerations to axisymmetric solutions. With this assumption, we need only use A, the ϕ component of the vector potential, to represent the magnetic field:

$$\boldsymbol{B} = \left(-\frac{\partial A}{\partial z}, \; 0, \; \frac{\partial A}{\partial r} + \frac{A}{r} \right) . \tag{5}$$

Unlike our various related papers on magnetoconvection, we will here display all variables in dimensional form. For this we need to select appropriate reference quantities to convert the dimensionless form of the p.d.e.'s as presented by HR to physical quantities. The dimensionless quantities that specify the model are θ, the initial temperature gradient; m, the polytropic index; γ, the ratio of specific heats; σ and ζ, the viscous and magnetic Prandtl numbers; R, the Rayleigh number at midlayer; and β_0, the plasma beta at $z = 0$, $r = 0$, which is the ratio of gas pressure to magnetic pressure.

Here we are interested in flows on the scale of supergranules. We will assert that the layer depth in the computational domain is 10 Mm, corresponding to roughly supergranular scales, and in accordance with the variation of ζ with depth. The mean density and temperature at the surface will be taken to be that of the photosphere, or 3×10^{-4} kg m^{-3} and 6000 K. The sound speed in the

photosphere is approximately 7 km s^{-1}, which sets a dimensionless time unit at 1400 s solar time.

3.1. *Boundary Conditions*

Our computational domain is a cylinder of radius Γ, so (r, z) satisfy

$$0 \le r \le \Gamma\ , \qquad 0 \le z \le 10\ \mathrm{Mm}\ , \tag{6}$$

with $z = 0$ at the photosphere. We require that all variables be sufficiently well behaved at the axis ($r = 0$) that the differential operators in the p.d.e.'s are nonsingular, thereby

$$A = u = \frac{\partial T}{\partial r} = \frac{\partial w}{\partial r} = 0 \quad \text{at} \quad r = 0\ , \tag{7}$$

where u, w are the radial and vertical velocity components.

At $z = 10$ Mm, we impose a constant-temperature, line-tied magnetic field and an impenetrable, stress-free surface:

$$T = 6000\ \mathrm{K}\left(1 + \frac{z}{10\ \mathrm{Mm}}\right)\ , \quad A = A_0(r)\ , \quad w = \frac{\partial u}{\partial z} = 0\ . \tag{8}$$

At the outer boundary $r = \Gamma$, we have no lateral heat flux across the slippery, perfectly conducting side wall:

$$A = \frac{\partial T}{\partial r} = u = \frac{\partial w}{\partial r} = 0\ . \tag{9}$$

At the photosphere, we apply a radiative and potential field condition. Specifically, we set

$$\frac{\partial T}{\partial z} \propto T^4\ , \qquad \frac{\partial A}{\partial z} = \mathscr{M}_{\mathrm{pot}}(A)\ , \tag{10}$$

where $\mathscr{M}_{\mathrm{pot}}(A)$ is a linear operator described by HR. The required coefficient in the radiative loss function is not Stephan's constant, rather it is a constant chosen to be consistent with our model. While we retain the functional form of blackbody radiative cooling, we are not imposing realistic solar heat fluxes, and thus we choose the proportionality constant such that the initial, unperturbed state of the system is a static solution to equations (1)–(4) and (8). Furthermore, we assume that this radiated energy has no influence on the overlying corona.

4. MAGNETOCONVECTION

Table 1 presents the parameter range we examined for our magnetoconvection model. Two relatively large aspect ratios were considered. These were chosen in an attempt to position the outer boundary away from where the magnetic flux returns from the corona. This met with limited success, however, as will be seen in the figures. Hence, this work focuses on the large cases with $\Gamma = 90$ Mm. The value of the initial field strength at the surface B_0 was also varied to span a range in total magnetic flux. The total flux entering through the bottom of the computational domain, Φ, is the amount of magnetic flux entering within the radius where the field reverses. It is completely specified by our choice of axial magnetic field B_0 and the horizontal extent of the computational domain Γ.

Figure 1 displays the evolution of a magnetoconvective solution with a magnetic flux $\Phi = 3.65 \times 10^{20}$ Mx ($Q = 300$) at five instants in time. The temperature fluctuation relative to the initial static state is shown as the color background, while the velocity is indicated by the small triangles, whose area is proportional to the local speed.

TABLE 1

SUMMARY OF SOLUTIONS

Γ (Mm)	Q	Φ ($\times 10^{18}$ Mx)	B_0 (gauss)
60	100	116	670
60	300	201	1200
60	1000	337	2000
90	100	211	670
90	300	365	1200
90	1000	667	2000

NOTE.—We consider two aspect ratios (Γ) and three values of Chandrasekhar numbers Q, which correspond to six values of emerging magnetic flux entering the bottom of the convecting layer, Φ. B_0 is the value of the initial magnetic field at $r = 0$ and $z = 0$. The Chandrasekhar number Q based on the axial field B_0 is included for comparison with previous work.

The magnetic flux is quickly expelled from the bulk of the convecting layer in a few overturn times. After this transient state, the solution slowly evolves toward an equilibrium state consisting of a central flux concentration surrounded by a collar flow, which is surrounded, in turn, by a second convective roll. This outer convective roll serves to pin the returning flux to the outer boundary. Within the central flux concentration, much weaker convection cells form, which can be identified with umbral dots. The overall structure of the flow is similar to the unipolar simulations of HR. The continuation of magnetic field lines into the corona is included in more detail in Figure 4 to show the overlying loop structure.

For weaker initial fields, the central flux tube becomes more concentrated, as seen previously by HR, and the flows appear to maintain a time-dependent behavior. In Figure 2 the flows in the region surrounding the flux tube when $\Phi = 2.11 \times 10^{20}$ Mx can be seen to dredge field up repeatedly, forming small dipolar structures. These structures are quickly compressed into narrow flux elements protruding through the upper boundary that are then rapidly advected in the direction of the flow within which they first appear. Thus, in the weak-field case the continual recycling of magnetic flux results in solutions that never relax to a completely steady state.

Stronger field solutions display time dependence for another reason. Figure 3 displays the results for a solution with $\Phi = 6.67 \times 10^{20}$ Mx. Now the central flux tube fills a significant fraction of the computational domain. The flows outside of this region attain a relatively steady state, while small convective cells form in its interior that migrate inward with time. These appear to be related to the magnetoconvective traveling wave solutions first described by Hurlburt, Matthews, & Proctor (1996).

Taken together, these three simulations seem to bracket the types of behaviors seen in the solar photosphere. For weak fields, porelike solutions form that possess little internal structure. As the flux increases, interior flows and small-scale traveling waves develop. We now will turn to considering how these differing dynamics relate to the evolution of coronal fields and to possible mechanisms for coronal heating.

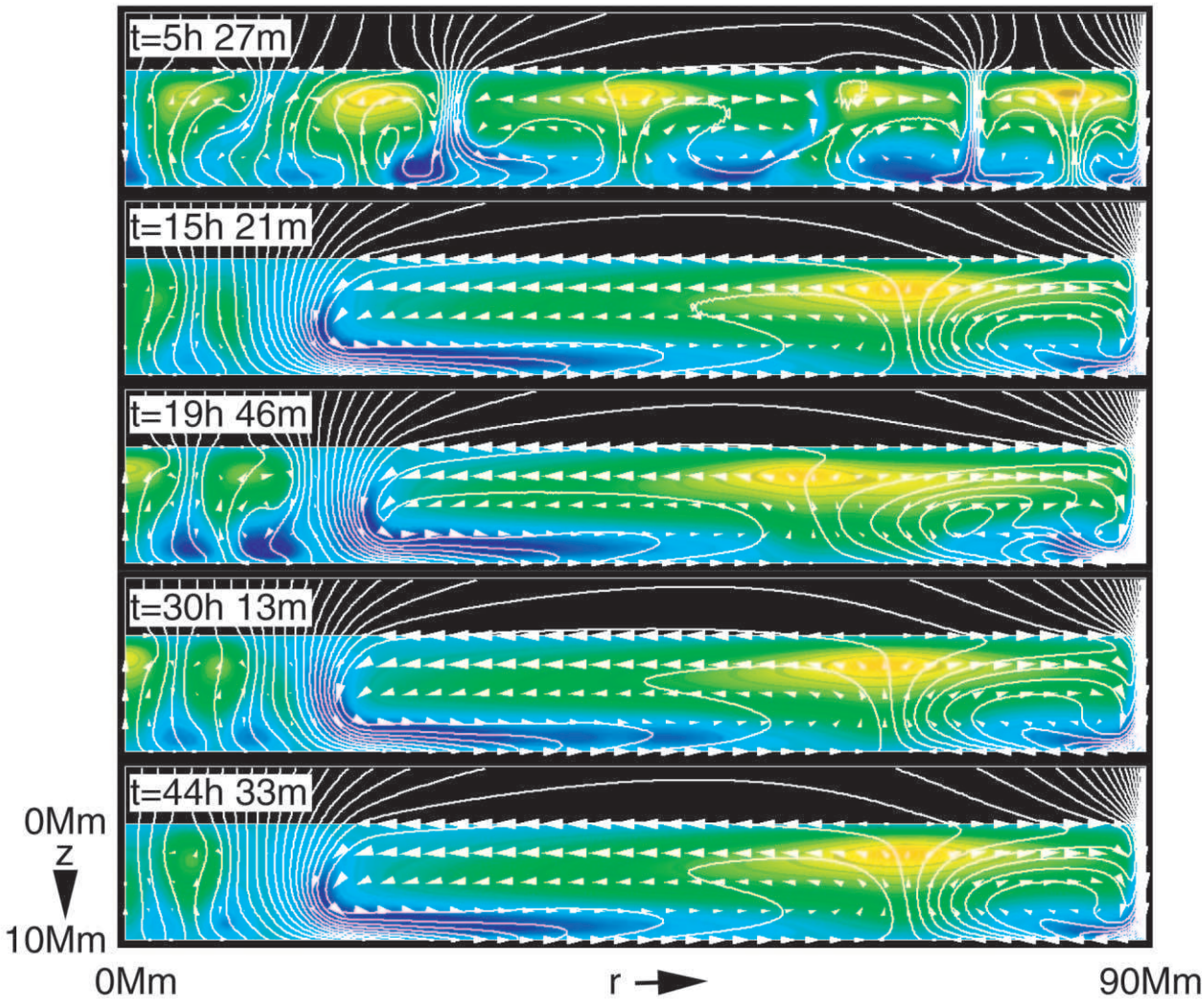

FIG. 1.—Magnetoconvective thermodynamics for $\Phi = 3.65 \times 10^{20}$ Mx ($\Gamma = 90$). After a period of transient behavior ($t < 20$ hr), the solutions settle down with flows sweeping the field to both ends of the computational domain. Near the axis (*left*) the flows are suppressed by the magnetic fields. However, small, weak convective features persist there and slowly migrate toward the axis.

5. CORONAL FIELDS

The choice of potential boundary conditions for the upper boundary in these simulations provides some guidance as to the evolution of "coronal" fields above this arbitrary "photosphere." The geometry and evolution of the field above the computational domain is completely specified by the distribution of the field at the photosphere. Returning to Figure 2, we can see the evolution of the coronal field for the case with $\Phi = 2.11 \times 10^{20}$ Mx. As the convection sweeps the field to the axis and outer boundary, the fields reconfigure themselves. The solution rapidly takes on the porelike structure discussed in the previous section. However, the nearly horizontal flux in the range $20 < r < 60$ Mm results in the repeated emergence of small bipolar structures as seen at time $t = 41$ hr. These emerging flux regions are associated with smaller scale eddies that sweep the flux into their corresponding downflows. These smaller scale cells interact with the previously established convection cells, causing a rapid reconfiguration of the magnetic field as they move away from the region of emergence.

The cases with $\Phi = 3.65 \times 10^{20}$ Mx and $\Phi = 6.67 \times 10^{20}$ Mx, displayed in Figures 1 and 3, quickly relax to a more stationary state after the flows rapidly sweep the field into the periphery. Figure 4 displays the long-term steady behavior of the nearly steady solution when $\Phi = 3.65 \times 10^{20}$ Mx. The final field attains a stationary state where the magnetic field lines are displaced upward from the potential configuration imposed in the initial static state.

It is difficult to compare these loops with observation for several reasons. Foremost is the fact that the Sun somehow selects specific field lines for heating and emission. The filamentary structure of the loops seen by the *Transition Region and Coronal Explorer* (*TRACE*), for instance, shows highly intermittent brightening of loops around active regions. In addition, comparisons between instruments sensitive to different coronal temperatures, such as *TRACE* and *Yohkoh*/SXT, show dramatically different structures. These facts serve as diagnostics for both models of coronal heating and models of the subphotospheric magnetoconvection that ultimately drives this heating. Models of coronal heating and magnetoconvection must match the selective emission seen in the corona. In the following section we present a pre-

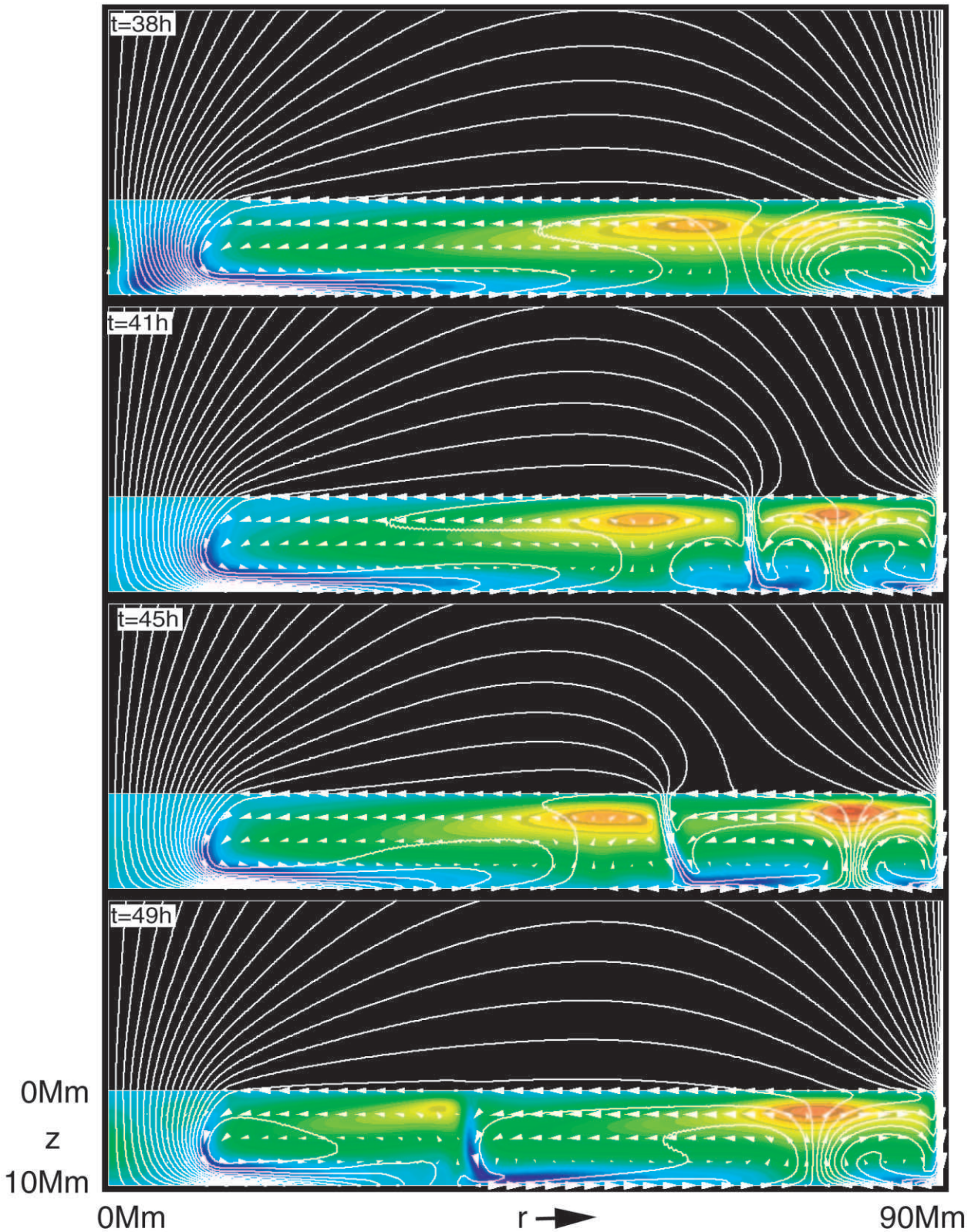

FIG. 2.—Magnetoconvective thermodynamics for $\Phi = 2.11 \times 10^{20}$ Mx displays persistent time dependence in the region surrounding the spot. Magnetic fields repeatedly rise to the surface, where they are concentrated and swept away by the convective flows.

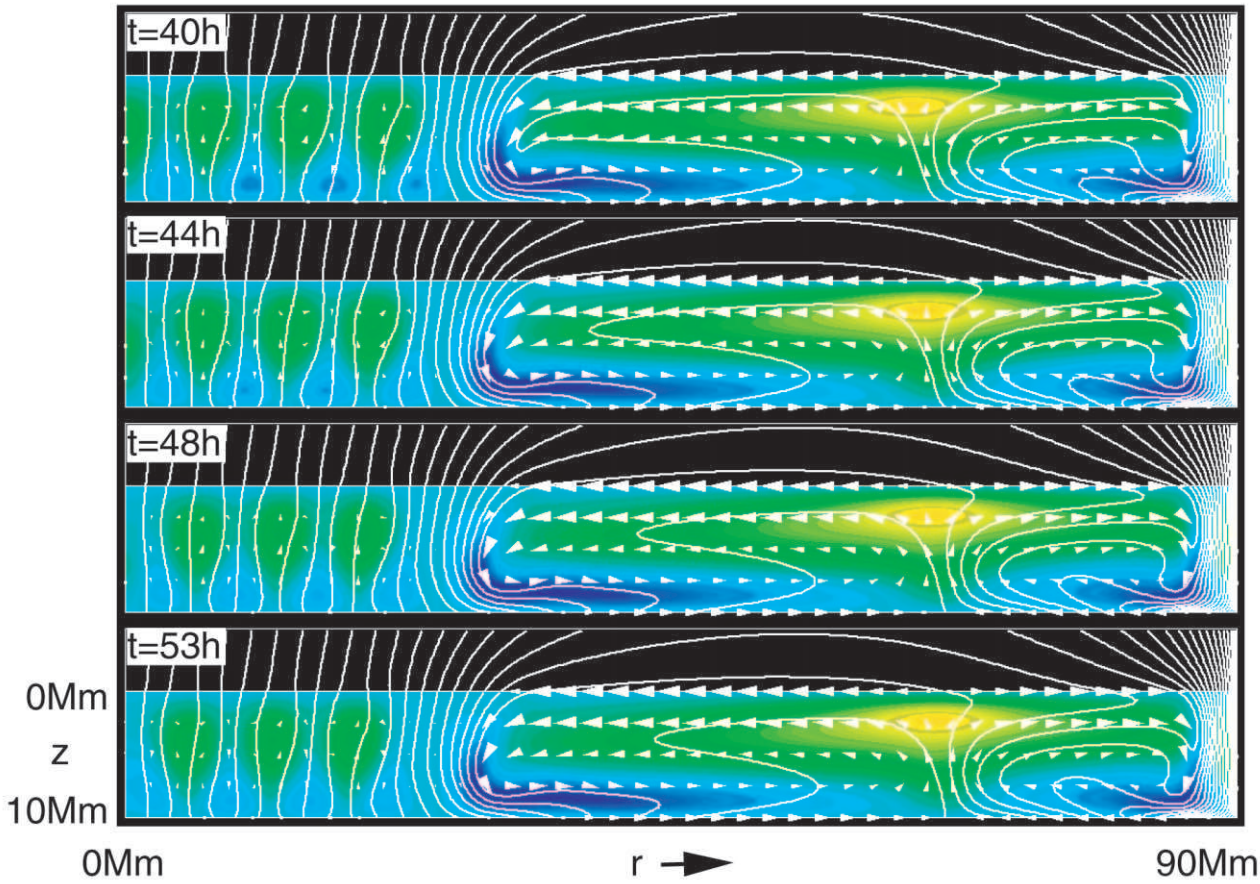

FIG. 3.—Magnetoconvective thermodynamics for $\Phi = 6.67 \times 10^{20}$ Mx forms a large region of concentrated magnetic field with several weak convection cells within it. The flows outside of this region attain a nearly steady state.

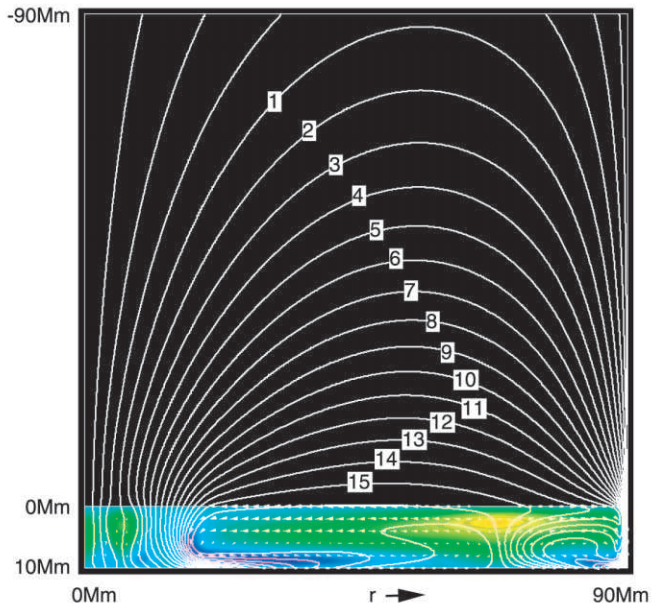

FIG. 4.—Coronal field lines for $\Phi = 3.65 \times 10^{20}$ Mx experience significantly different motions at their footpoints. Fields near the axis (numbered 1–10) are displaced periodically by the weak convection cells within the model sunspot. Field lines near the edge of the spot (lines 11–15) experience the strong converging flows that are confining the spot.

liminary parameterization for this heating and compare the resulting coronal emissions with what would be observed by *TRACE* and SXT.

6. HEATING THE CORONA

Our model asserts that the coronal fields above our magnetoconvective layer are potential and axisymmetric. This is not too far from what is observed on the Sun—at least in cases where the evolution of the magnetic footpoints in the photosphere moves slowly relative to the response time of the corona. In our model, the coupling between the dynamics of the magnetoconvection and the heating of the overlying corona is provided by the Poynting flux entering the coronal structures. The surface distribution of the Poynting flux in our magnetoconvection calculation (at $t = 0$) is shown in Figure 5 for the three choices of magnetic flux, as specified by the Chandrasekhar number, Q. There is a large variation in the available energy entering the corona at different locations within the simulated sunspot, which will have a marked bearing on the heating observed in the coronal loops.

Strictly speaking, the fact that the photospheric boundary conditions, and consequently the coronal field, are potential requires that all of the energy supplied by the Poynting flux translate into a change in the total magnetic energy contained in the coronal field. The condition that the corona responds to the changing boundary via a series of potential

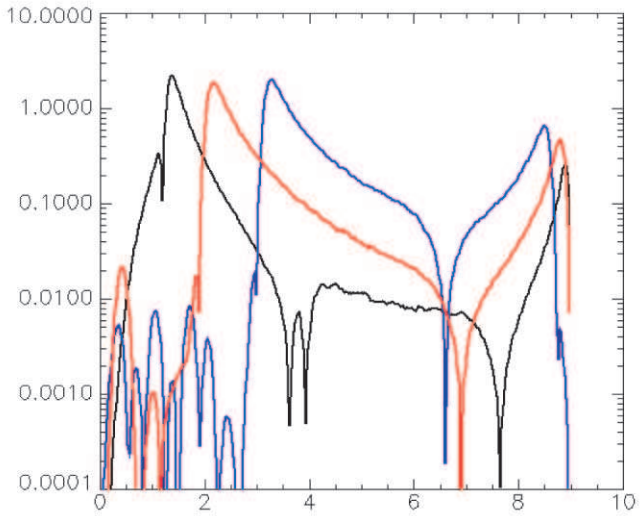

FIG. 5.—Radial distribution of Poynting flux for $Q = 100$ (*black*), 300 (*red*), and 1000 (*blue*).

configurations provides no mechanism for producing the additional energy required to heat the corona. The Sun, however, must contrive to dissipate some of the available magnetic energy as heat in order to attain the MK temperatures we detect. The amount of energy required for this heating, while large by coronal standards, is negligible relative to the energy residing in the convection region. Hence, we postulate that the requisite energy can be dissipated with negligible consequences for the subphotospheric flows and, subsequently, the potential nature of the coronal field.

We assume a heating function, E_H ergs cm^3 s^{-1}, which is a fixed, but small, fraction of the total Poynting flux entering the loop, viz.,

$$E_H = \chi P_{\rm tot}(r_a; r_b) , \tag{11}$$

where $P_{\rm tot} \equiv (\boldsymbol{E} \times \boldsymbol{B})_{\rm tot}$ is the total Poynting flux entering the corona through the surface at $z = 0$, $(r_a; r_b)$ represent the radial distances from the sunspot axis of each of the field-line footpoints, and χ signifies the small fraction of the Poynting flux that gets dissipated as heat and distributed throughout the loop. The Poynting flux is given by the interaction of the flows and magnetic field at the surface via $\boldsymbol{E} = \boldsymbol{v} \times \boldsymbol{B}$; there is no intrinsic electrical field.

Equation (11) indicates how we relate the total heating rate on a given field line to the dynamics of the magnetoconvection. However, in order to determine the distribution of physical parameters along each loop, we need to adopt a spatial dependence for the heating. In our previous papers (Alexander, Hurlburt, & Rucklidge 1999; Hurlburt, Alexander, & Rucklidge 2000) we have restricted our analysis to uniform heating with $E_H(s) =$ constant, following Rosner, Tucker, & Vaiana (1978). However, this is inappropriate for loops that extend to heights above the pressure scale height (cf. Serio et al. 1981) and is not consistent with recent observational findings (e.g., Aschwanden, Nightingale, & Alexander 2000b). We, therefore, parameterize the heating function with a base heating rate, E_{H0}, and an exponential scale height, s_H, viz.,

$$E_H(s) = E_{H0}(s)e^{-s/s_H} , \tag{12}$$

where s is the loop coordinate and we apply equation (12) to each loop. Note that E_{H0} is not a free parameter but is determined directly from the Poynting flux and the fraction χ (eq. [11]).

This choice of a footpoint heating function has recently been supported by observations (Aschwanden et al. 2000a; Aschwanden, Schrijver, & Alexander 2001). These authors have demonstrated that EUV loops observed with *SOHO*/EIT and *TRACE* can be in hydrostatic equilibrium only if the heating is concentrated in the lower 10–20 Mm of the corona. We have utilized the results from a hydrostatic analysis developed by Schrijver & Aschwanden (2002) to obtain explicit solutions for the temperature and density along the loops. Although Aschwanden et al. (2000a; 2001) found that many of the observed temperature and density distributions within coronal loops required that they be in an intrinsically dynamic state, the quasi-static assumption adopted here is adequate given the exploratory nature of this hybrid sunspot model.

The details of the dissipation of the magnetic energy into heat are beyond the scope of this work. However, we can relate our assumptions to existing ideas about coronal heating. As an example, we might assume some form of wave heating mechanism (although current dissipation models should not be ruled out, e.g., Mandrini, Demoulin, & Klimchuck 2000). Because of the large atmospheric density stratification from the photosphere to the corona, coronal loops can act like interference filters for waves that are generated in the convection zone, travel through the solar atmosphere to the corona, then return to the convection zone (e.g., Ionson 1978; 1982; Hollweg 1981). The presence of an interference filter gives rise to resonant transmission peaks in the frequency domain that allow the necessary large energy fluxes (10^4 W m^{-2} for active regions; Withbroe 1988) to enter the loops. The key to the peak transmission frequency is the length of the resonant cavity, which, in our case, would be the length of the coronal loop. The differing coronal loop lengths result in different loops being sensitive to a different part of the wave power spectrum available.

The efficiency of resonant absorption of Alfvén waves has been studied by a number of authors, e.g., Davila (1987), Hollweg & Yang (1988), Ofman & Davila (1995), and Poedts et al. (1997). All of these studies show that resonant absorption of Alfvén waves is a viable heating mechanism for solar coronal loops, provided that there is enough power available in the wave frequency ranges. Beliën, Martens, & Keppens (1999) have recently demonstrated that only a few percent of the power supplied by the Poynting flux entering a coronal loop is converted into heat via the resonant absorption of Alfvén waves. It should be noted that the model of Beliën et al. (1999) contains a complete atmosphere and that resonant heating is significantly more efficient (heating is 4–8 times higher) in the chromosphere and transition region than in the corona. The lack of a chromosphere and transition region in our model loop atmosphere means that we overestimate the Poynting flux flowing into the corona by as much as 40%. However, we assume that this factor can be embedded in the scaling constant, χ.

The distribution of temperature and density in the coronal portion of our sunspot system is determined from the usual quasi-static energy equation,

$$\frac{dF_c}{ds} = E_H(s) - \frac{\hat{\Lambda}(T)p^2}{4k^2T^2} , \tag{13}$$

where s is the arc length along a flux tube, T is the tempera-

ture, F_c is the thermal conductive flux, $A(s)$ is the tube cross-sectional area, p is the pressure, $\Lambda(T)$ signifies the temperature-dependent radiative loss function (cf. Tucker & Koren 1971; Rosner et al. 1978), k is the Boltzmann constant, and

$$\frac{dT}{ds} = -\frac{F_c}{\kappa_0 T^{5/2}} \tag{14}$$

with $\kappa_0 \simeq 10^{-6}$ ergs s^{-1} cm^{-1} K$^{-7/2}$ is the coefficient of thermal conductivity. The heights of the loops are determined by the scale of the sunspot penumbra and the inclination of the field at each point, r. Some of the loops modeled here have heights larger than the pressure scale height for a 1 MK plasma ($\lambda_p \sim 46$ Mm). The pressure in each loop cannot, therefore, be assumed constant, and so we use

$$p(s) = p_0 e^{-h(s)/\lambda_p} , \tag{15}$$

where p_0 is the base pressure, $h(s)$ is the height above the surface, and $\lambda_p(T(s))$ is the pressure scale height. We further adopt the ideal gas law such that $n(s) = p/2kT$.

The quasi-static assumption is justified here since (1) all of the flows generated in the photosphere by the convection are purely orthogonal to the field with no component up into the corona and (2) the convective rollover time is long enough (1–2 hr) for the loops to reach equilibrium.

The total energy available for heating the loops is assumed to be directly proportional to the total Poynting flux entering the loop from the base. This energy is then distributed throughout the loop volume per equation (12). In order to test the effect of the heating scale height s_H, we present solutions for $s_H \in [10,\ 30]$ Mm. Rather than arbitrarily specifying the constant fraction, χ, of the Poynting flux dissipated as heat in the coronal loops, we determine it from the requirement that at least one of the loops in our system attains a maximum temperature of 1 MK. This is accomplished by adopting a scaling of $\chi = 3.2 \times 10^{-4}$, which results in the apex temperature of loop 1 (see Fig. 6) reaching 1 MK at the end of its calculated evolution when the system has reached a steady state. The fact that $\chi \ll 1$ is consistent with our earlier statements that the energy required to heat the corona can be dissipated with negligible consequences for the coronal field configuration. The chosen value of χ was determined assuming a heating scale height of $s_H = 30$ Mm. The corresponding base heating rate is $E_{H0} = 4.5 \times 10^{-5}$ ergs cm^{-3} s^{-1}. Thereafter, the heating in all other loops at all other times and with all other heating scale heights is assumed to result from the same fraction of the Poynting flux entering the loop. Adopting the same fraction for the $s_H = 10$ Mm solutions provides a direct comparison with the equivalent $s_H = 30$ Mm solutions; with $s_H = 10$ Mm, loop 1 at time $t = 41$ hr 33 minutes has a maximum temperature of $T_{\max} = 0.52$ MK and a base heating rate of $E_{H0} = 1.27 \times 10^{-4}$ ergs cm^{-3} s^{-1}.

In Figure 6 we show the temperature distributions in each of the loops for the sunspot model with $Q = 300$ at late times when the solution had converged to a steady state. There is a marked variation between the two cases. In comparing temperature profiles between Figures 6*a* and 6*b* it should be noted that, while there is a wide variation of the total heating within a given set of loops, equivalent loops can be directly compared. The first thing to notice is that regardless of the distribution of the heating, the different loops attain a wide variety of coronal temperatures with the longer scale height resulting in higher maximum temperatures. Second, the degree of isothermality of the coronal portion of the loops increases as we move to smaller heating scale heights. Finally, we note that the choice of energy flux dissipation, χ, allows for the presence of cool loops with $T_{\max} \sim 0.5$ MK in the small scale height solutions. It is important to note that the scaling, χ, is the same for all loops in our model. This is equivalent to the assumption that each loop has the same ability to tap into the energy provided by the Poynting flux, a property that would depend strongly on the particular heating mechanism responsible for heating the loop. Values of χ that vary from loop to loop may be incorporated in future work to investigate the role of different heating mechanisms that will have different dissipation properties.

We show the variation of the maximum loop temperature with time for two loops identified in Figure 4 and for two heating scale heights in Figure 7. In all cases, the initial start-up transient of the magnetoconvection, as it evolves from the random initial conditions to a relatively stable state, results in large temperature swings. These swings are primarily a response to dramatic restructuring of the fields

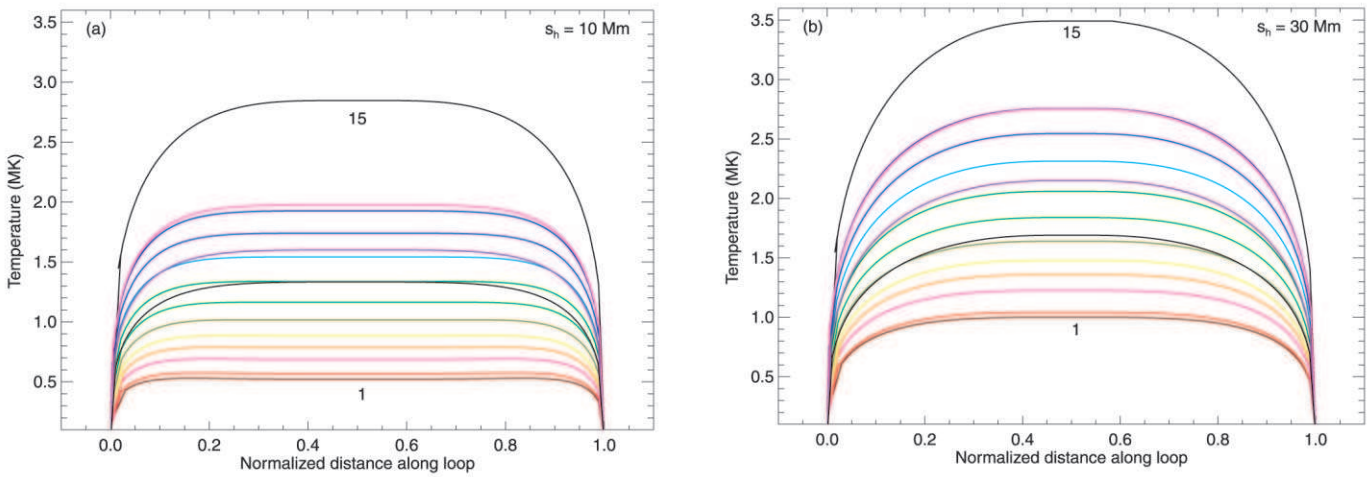

FIG. 6.—Temperature profiles for each of the field lines identified in Fig. 4. Each panel represents a heating rate with a different heating scale height: (*a*) $s_H = 10$ Mm, (*b*) $s_H = 30$ Mm.

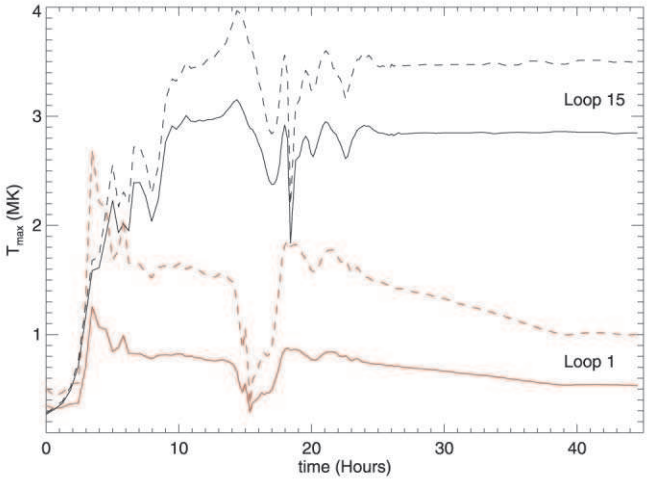

FIG. 7.—Variation of loop apex temperatures with time for loops 1 and 15 from Fig. 6 with $s_H = 10$ Mm (*solid lines*) and $s_H = 30$ Mm (*dashed lines*).

during the evolution to stable structures (compare to the corresponding times in Fig. 1). After approximately 20 hr, when a stable spot has formed, the peak temperatures decay toward stable values. The heating profiles are displayed for representative times (the same as those in Fig. 1) in Figure 10.

7. OBSERVATIONAL DIAGNOSTICS

The combination of a sunspot model, whereby the surface field is completely specified, with a coronal heating model, in which plasma parameters are determined for a given energy input, allows us to explore the role of convection region dynamics in generating the observed coronal emission characteristics. The comparison of expected emissions from different telescopes provides a diagnostic capability for investigating the heating function in these loops. The temperature and density distributions generated from a solution to the quasi-static energy equation (13) allow us to specify completely the emission expected in the various channels (filters) of the *TRACE* (SXT) telescope through knowledge of their respective temperature response functions:

$$\mathscr{F}_i(T) = A \int_s n(s)^2 G_i(T) ds \, .$$

$\mathscr{F}_i(T)$ is the flux expected in *TRACE* channel i (or SXT filter i), A is the loop cross-sectional area, n is the electron density, $G_i(T)$ is the appropriate response function, and ds is the element of the loop at temperature T.

Figure 8 shows the expected distribution of emission from the coronal flux tubes in the 171 and 195 Å lines of *TRACE* (see Handy et al. 1999) and the Al.1 filter of *Yohkoh*/SXT (Tsuneta et al. 1991) for two values of the heating scale height, which generate maximum temperatures in the ranges 0.52–2.9 and 1–3.5 MK, respectively. The distinctly different patterns of emission in the different instruments present a diagnostic capability for investigating coronal heating. In particular, we note that the X-ray emission is confined to a hot core of compact loops that are overlain by long cool EUV loops. It is also apparent that the distribution of Poynting flux at the coronal base results in a nonuniform distribution of the emission with particular loops highlighted (Fig. 9). The combination of distinct distributions of emission in the different temperature regimes allows for a more quantifiable comparison with observation.

Another potentially useful diagnostic is the observation of time variability in the coronal loops. Associating this behavior with the dynamical development of the input

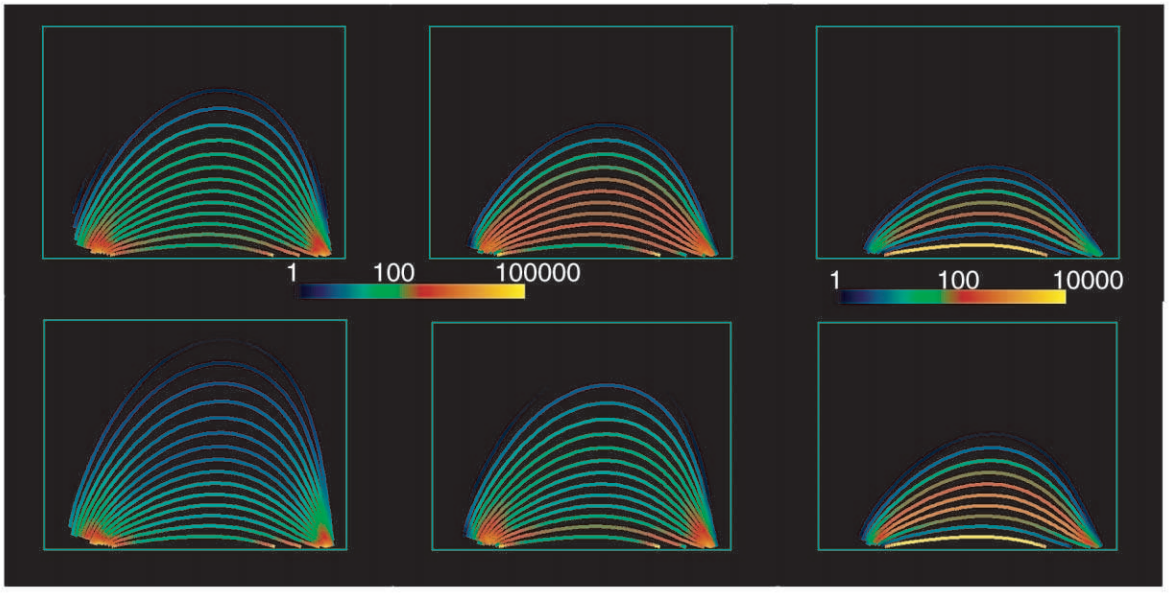

FIG. 8.—Emission characteristics for temperature distributions shown in Fig. 6. The upper panels represent a heating scale height of $s_H = 10$ Mm, while $s_H = 30$ Mm in the lower panels. In each row we show the *TRACE* 171 Å, *TRACE* 195 Å, and SXT/Al.1 emission distributions, respectively, from left to right.

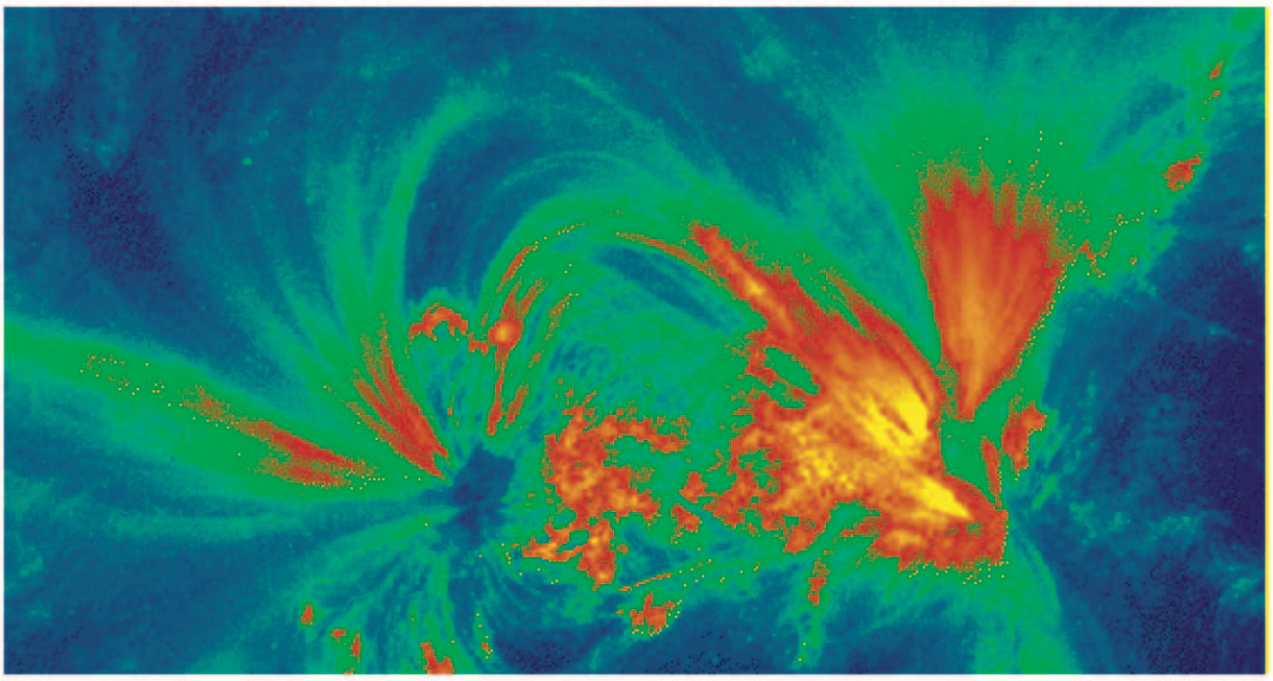

FIG. 9.—*TRACE* 171 Å image of NOAA AR 9017 on 2000 June 2. One can see various sets of loops distributed nonuniformly. Compare with the top left panel of Fig. 8.

energy (i.e., the Poynting flux at the base) provides a natural tie-in to and diagnostic tool for the magnetoconvective processes. As the magnetoconvection progresses, the input flows alter the $\boldsymbol{v} \times \boldsymbol{B}$ forces at the base of the field lines, which in turn results in a change of the heating via the coronal dissipation of a "constant" fraction of the varying Poynting flux. The timescale for the variation of the Poynting flux is on the order of a convection cell rollover time ($\sim$1–2 hr), while a typical response time for coronal loops is significantly faster. Consequently, we assume that the "steady state" energy input at each time is determined by the instantaneous value of the Poynting flux.

Figure 10 displays the distinct time development in the three coronal channels for the parameters chosen here. Once again we can see significant differences between the EUV and soft X-ray emission. The bulk of the X-ray emission is centered on the hot compact loops as highlighted in Figure 8. The temporal development of the coronal emission exhibits a number of interesting properties. First, the magnetoconvection causes a transfer of the bulk of the heating toward the shorter core loops with time, resulting in an active region in which a hot core of compact loops is surrounded by longer cooler loops. This is often observed in active regions targeted by both SXT and *TRACE*. An example is shown in Figure 11.

Second, the progression of the heating with time results in an apparent upward motion of bright loops, despite the fact that the field lines are not varying significantly in position. This is a direct result of the time-varying injection of energy from the magnetoconvective motions at the surface boundary. This sort of behavior can often be seen in *TRACE* movies of the nonerupting active region corona. The timescales in Figure 10 are fairly long but do indicate the diagnostic capability of the dynamically varying data for yielding information on the coronal heating process.

8. SUMMARY AND DISCUSSION

The coupling of the motions within and below the solar photosphere to the chromosphere and corona is one of the fundamental issues in solar physics. Our long-term goal is to understand this coupling through the development of numerical models that can be directly compared with observation. In this paper we have presented preliminary results that show the potential for this line of research.

The key to the approach taken here is that we assume a direct relationship between the dynamics of the subphotospheric magnetoconvection and the dynamic heating of distinct flux tubes in the solar corona. This generates a wide variety of observational signatures that can be tested against current observations of active regions by instruments aboard *TRACE*, *SOHO*, and *Yohkoh*. (In this work the emission expected in the *SOHO*/EIT would be only slightly different from that seen in *TRACE* because of the different sensitivities.)

Our survey of magnetoconvective solutions with differing amount of magnetic flux ranges between porelike solutions with small total magnetic flux (cf. HR) and the magnetoconvective traveling wave solutions (cf. Hurlburt et al. 1996) at large total flux. All three cases considered exhibit an enhanced heating at the umbra/penumbra boundary with the radial position of this "collar" increasing as the total flux increases. For the porelike solutions ($\Phi = 2.11 \times 10^{20}$ Mx; Table 1) the heating falls off more slowly and with less structure as we move deeper into the umbra, with the consequence (not shown) that larger loop structures will receive significant and comparable heating. This manifests as diffuse emission surrounding a brighter and hotter core, similar to that depicted in Figure 8. The weak, traveling convective motions with our model umbra for the higher flux cases

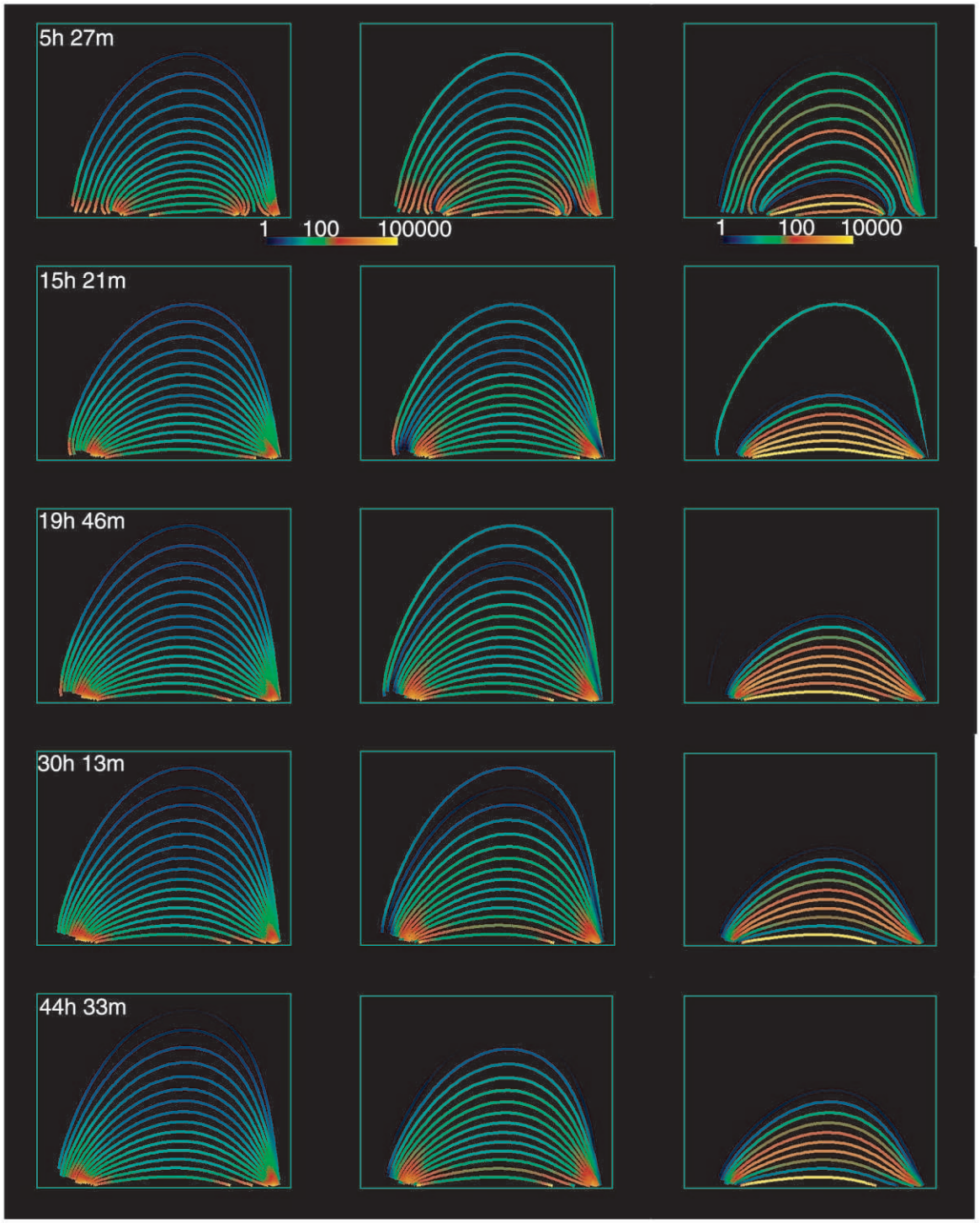

FIG. 10.—Time development of emission in the *TRACE* 171 and 195 Å channels (*left and center columns*) and the SXT Al.1 filter (*right column*). The *TRACE* and SXT sequences are scaled independently, with the flux in DN s^{-1} shown.

may induce apparent rising motion in the relatively static coronal fields as the location of maximum Poynting flux migrates inward.

In our coronal modeling we considered two different heating scale heights, $s_H = 10$ Mm and $s_H = 30$ Mm, with the results shown in Figures 6 and 8. The solutions with the larger heating scale height exhibited hotter loops with stronger temperature gradients (Fig. 6). As the heating scale height increases, the overlying loop structures start to appear in the *TRACE* 171 Å channel while the lower lying loops appear brighter in the *TRACE* 195 Å and SXT channels (Fig. 8). The often observed appearance of large cool loops surrounding a hot compact core is enhanced at the larger scale heights. This is consistent with the general trend of the hydrostatic solutions approaching the uniform heating solutions of Rosner et al. (1978) or Serio et al. (1981) as the ratio of scale height to loop length, s_H/L, increases (see Aschwanden & Schrijver 2002).

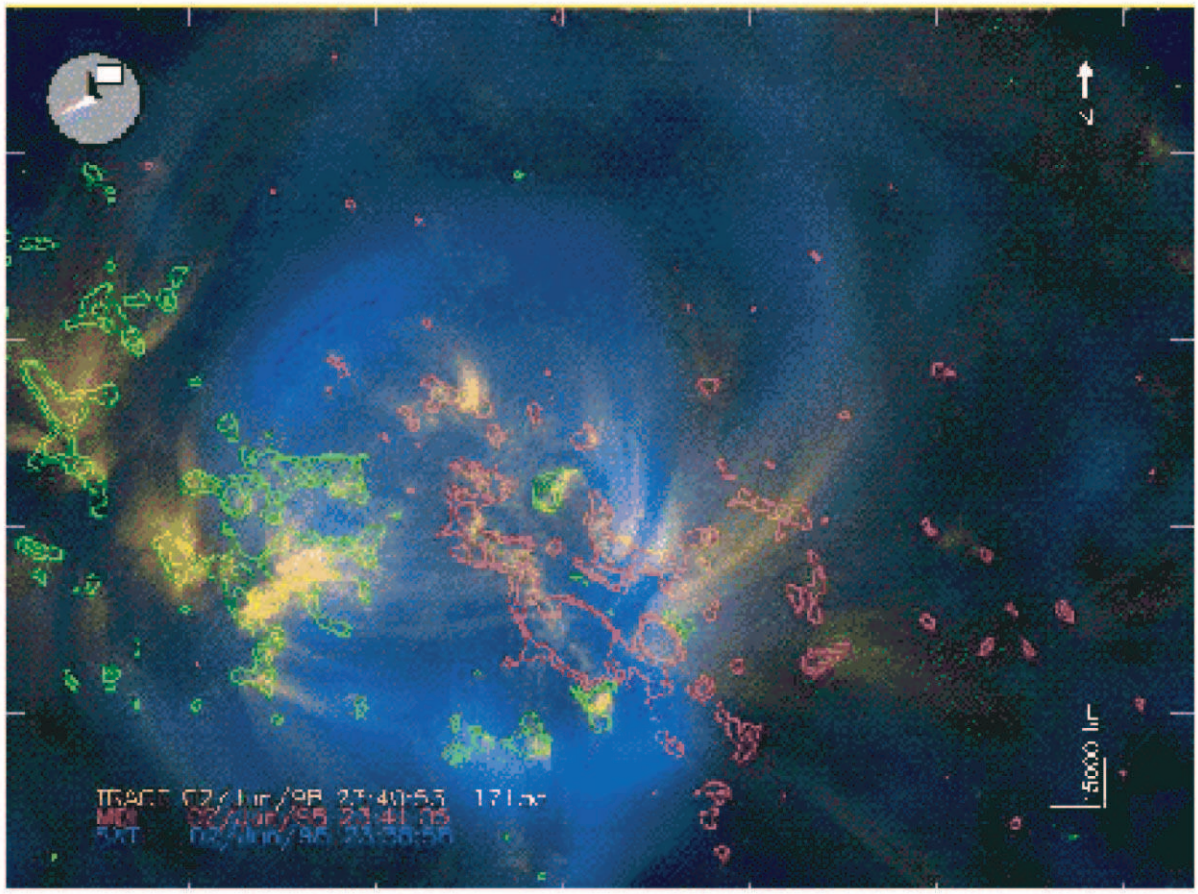

FIG. 11.—Observation of an active region by the *TRACE* 171 Å filter (*yellow*) and SXT (*blue*) with surface magnetic field provided by *SOHO*/MDI (*green*/*red*). Figure courtesy of R. Nightingale.

These results indicate that a coupled model, where the subphotospheric physics has a direct and well-understood impact on the radiation and dynamics of the corona, allows us to utilize the wealth of coronal observations, in space, time, and temperature, to gain insight into the physics of magnetoconvection. Moreover, it provides a direct link between the energy generation, as subphotospheric and photospheric kinematics, and its dissipation, as heating and dynamics in coronal loops, allowing us not only to investigate the viability of different loop heating models but to explore the heating of active regions as part of a single distribution of coupled processes. Determining the reason for the observed spatial distribution of heated loops in a coronal volume is as important, if not more so, as determining the heating mechanism for individual loops. Only by modeling full active regions and determining their relationship to the source of the energy can we truly say that we understand the coronal heating problem. The present paper takes a first step in that direction by addressing the direct relationship between the subphotospheric dynamics and the spatial distribution of heated coronal loops.

Future work will see the development of a more detailed coupling between the subphotospheric and coronal regimes. This will require the inclusion of a chromosphere and transition region as well as a means to include more feedback from the coronal behavior to the model of magnetoconvection. A fully time-dependent heating model incorporating flows is also a necessary step if we are to achieve these goals.

Once all of the necessary enhancements to the model are in place, a detailed comparison with photospheric and coronal observations, more rigorous than the qualitative comparison presented here, will be possible. Having such a fully integrated model of something as complex as a sunspot will allow us to gain significant insight into the physics governing the subphotospheric dynamics of sunspots and into the nature of magnetoconvection in general.

We wish to thank N. Weiss, M. Proctor, A. Title, R. Shine, and T. Tarbell for their insights and observations, R. Rauwendaal for assisting in the computations, and M. Aschwanden for discussion about the hydrostatic atmosphere calculations. This work was supported by NASA through grant NAG5-7376 at Lockheed Martin and grant NAG5-3077 at Lockheed Martin and Stanford. A. M. R. is grateful for support from the Royal Astronomical Society.

REFERENCES

Alexander, D., Hurlburt, N. E., & Rucklidge, A. M. 1999, in Proc. *SOHO* 8, Plasma Dynamics and Diagnostics in the Solar Transition Region, ed. J.-C. Vial & B. Kaldeich-Schürmann (ESA SP-446; Noordwijk: ESA), 117
Aschwanden, M. J., Alexander, D., Hurlburt, N. E., Newmark, J. S., Neupert, W. M., Klimchuk, J. A., & Gary, G. A. 2000a, ApJ, 531, 1129
Aschwanden, M. J., Nightingale, R. W., & Alexander, D. 2000b, ApJ, 541, 1059
Aschwanden, M. J., & Schrijver, C. J. 2002, ApJS, in press
Aschwanden, M. J., Schrijver, C. J., & Alexander, D. 2001, ApJ, 550, 1036
Beliën, A. J. C., Martens, P. C. H., & Keppens, R. 1999, ApJ, 526, 478
Davila, J. M. 1987, ApJ, 317, 514
Handy, B. N., et al. 1999, Sol. Phys., 187, 229
Hollweg, J. V. 1981, Sol. Phys., 70, 25
Hollweg, J. V., & Yang, G. 1988, J. Geophys. Res., 93, 5423
Hurlburt, N. E., Alexander, D., & Rucklidge, A. M. 2000, in IAU Symp. 203, Recent Insights into the Physics of the Sun and Heliosphere: Highlights from *SOHO* and Other Space Missions, ed. P. Brekke, B. Fleck, & J. B. Gurman (San Francisco: ASP), 106
Hurlburt, N. E., Matthews, P. C., & Proctor, R. E. 1996, ApJ, 457, 933
Hurlburt, N. E., & Rucklidge, A. M. 2000, MNRAS, 314, 793 (HR)
Ionson, J. A. 1978, ApJ, 226, 650
———. 1982, ApJ, 254, 318
Leka, K. D. 1997, ApJ, 484, 900
Lites, B. W., Elmore, D. F., Segraves, P., Skumanich, A. P. 1993, ApJ, 418, 928
Mandrini, C. H., Demoulin, P., & Klimchuck, J. A. 2000, ApJ, 530, 999
Martens, P. C. H., Hurlburt, N. E., Title, A. M., & Acton, L. W. 1996a, ApJ, 463, 372
Ofman, L., & Davila, J. M. 1995, J. Geophys. Res., 100, 23427
Poedts, S., Toth, G., Beliën, A. J. C., & Goedbloed, J. P. 1997, Sol. Phys., 172, 45
Rosner, R., Tucker, W. H., & Vaiana, G. S. 1978, ApJ, 220, 643
Schrijver, C. J., & Aschwanden, M. J. 2002, ApJ, 566, 1147
Schrijver, C. J., et al. 1999, Sol. Phys., 187, 261
Serio, S., Peres, G., Vaiana, G. S., Golub, L., & Rosner, R. 1981, ApJ, 243, 288
Sobotka, M., Brandt, P. N., & Simon, G. W. 1997, A&A, 328, 689
Sobotka, M., & Sütterlin, P. 2001, A&A, 380, 714
Title, A. M., Frank, Z. A., Shine, R. A., Tarbell, T. D., Topka, K. P., Scharmer, G., & Schmidt, W. 1993, ApJ, 403, 780
Tsuneta, S., et al. 1991, Sol. Phys., 136, 37
Tucker, W. H., & Koren, M. 1971, ApJ, 168, 283
Withbroe, G. L. 1988, ApJ, 325, 442
Zhao, J., Kosovovich, A. G., & Duvall, T. L., Jr. 2001, ApJ, 557, 384